applied sciences

MDPI

Review

A Review of Tunable Orbital Angular Momentum Modes in Fiber: Principle and Generation

Lipeng Feng, Yan Li *, Sihan Wu, Wei Li, Jifang Qiu, Hongxiang Guo, Xiaobin Hong, Yong Zuo and Jian Wu *

The State Key Laboratory of Information Photonics and Optical Communications, Beijing University of Posts and Telecommunications, Beijing 100876, China; 15201017279@bupt.edu.cn (L.F.); sihanwu@bupt.edu.cn (S.W.); w_li@bupt.edu.cn (W.L.); jifangqiu@bupt.edu.cn (J.Q.); hxguo@bupt.edu.cn (H.G.); xbhong@bupt.edu.cn (X.H.); yong_zuo@bupt.edu.cn (Y.Z.)

* Correspondence: liyan1980@bupt.edu.cn (Y.L.); jianwu@bupt.edu.cn (J.W.)

Received: 1 April 2019; Accepted: 17 May 2019; Published: 13 June 2019

Abstract: Orbital angular momentum (OAM) beams, a new fundamental degree of freedom, have excited a great diversity of interest due to a variety of emerging applications. The scalability of OAM has always been a topic of discussion because it plays an important role in many applications, such as expanding to large capacity and adjusting the trapped particle rotation speed. Thus, the generation of arbitrary tunable OAM mode has been paid increasing attention. In this paper, the basic concepts of classical OAM modes are introduced firstly. Then, the tunable OAM modes are categorized into three types according to the orbital angular momentums and polarization states of mode carrying. In order to understand the OAM evolution of a mode intuitively, three kinds of Poincaré spheres (PSs) are introduced to represent the three kinds of tunable OAM modes. Numerous methods generating tunable OAM modes can be roughly divided into two types: spatial and fiber-based generation methods. The principles of fiber-based generation methods are interpreted by introducing two mode bases (linearly-polarized modes and vector modes) of the fiber. Finally, the strengths and weaknesses of each generation method are pointed out and the key challenges for tunable OAM modes are discussed.

Keywords: orbital angular momentum; tunable OAM; Poincaré sphere; state of polarization

1. Introduction

A light beam has two "rotational" degrees of freedom: spin angular momentum (SAM) and orbital angular momentum (OAM) [1]. The SAM per photon is $\sigma\hbar$ (where $\hbar$ is the Plank's constant h divided by 2π), which is related to the state of polarization for left-circular $\sigma = +1$, for right-circular $\sigma = -1$, while for linearly polarized light $\sigma = 0$. For elliptically polarized light, the SAM varies from zero to $\pm 1\hbar$ as the state of polarization varies from linear to circular. The OAM is associated to the phase structure of the complex electric field with a helical phase front defined by the factor of $\exp(il\theta)$, which carry a definite amount of OAM per photon equal to lh. As the OAM beams have a phase singularity, they have a doughnut-shaped spatial profile with zero intensity at the center. Considerable interest in orbital angular momentum arises over its potential applications in multiple fields. For instance, orbital angular momentum can be transferred to trapped suitable material particles causing them to rotate, which enables optical manipulation, trapping and tweezers in fields as diverse as biosciences and micromechanics [2–5]; the angular momentum of light can be used to encode quantum information that is carried by the corresponding photon states [6]; the exploitation of the orbital angular momentum also opens the door to the generation and manipulation of multi-dimensional quantum entangled states with an arbitrarily large number of entanglement dimensions [7–10]; the doughnut

intensity profile and phase singularity of OAM contribute to contrast enhancement techniques by depleting the fluorescence everywhere except at the dark center of the depletion beam, which enables resolution microscopy beyond the diffraction limit [11–13]; the OAM modes are also applied in optical communications (fiber and free space) with large capacity and long ranges due to its partial robustness against turbulence [14,15]; and astrophysical processes may generate photonic OAM, such as light scattering off inhomogeneities in the environments surrounding energetic sources (masers, pulsars, quasars) and light scattering off rotating black holes [16], etc.

The unique advantage of using optical OAM in these applications relies, to a large extent, on the use of multiple different OAM states. For example, the multiple available OAM states facilitate high-dimensional quantum information processing and large-capacity optical communications. The rotation speed of the trapped micro-particles for optical micro-manipulation is also related to the states of OAM and required to be continuously adjusted [17,18]. Thus, the control of the orbital angular momentum in a beam is important.

In this paper, an overview of the basic concepts and generation methods of the tunable OAM modes is given. Firstly, the classical OAM mode is introduced in the Section 2, including the physical concept, mathematical expression and generation methods. Secondly, the basic concepts and theoretical expressions of three kinds of tunable OAM modes are briefly described in Section 3. In order to intuitively understand the OAM evolution, three Poincaré spheres (PSs) are used to represent the three kinds of tunable OAM modes, which is similar to the polarization PS. In addition, the relationships among three PSs are concluded. Then, the fiber-based and free-space generation methods are respectively classified into three types according to the controllable variables in the Section 4. Finally, the advantages and disadvantages of each generation method are listed and the key challenges for tunable OAM modes are discussed in Section 5.

2. The Classical Orbital Angular Momentum (OAM) Mode

The light beams carrying orbital angular momentum are spatially structured beams with helical phase fronts. For the points on the mode cross-section with the same radius, the polarization states and amplitudes are the same, but with different phases. The electromagnetic field of an classical OAM beam is identified by a phase term expressed as $\exp(\pm il\theta)$, where θ is the azimuthal angle in the transverse plane of the mode. The l which called as the topological charge means the number of 2π phase shifts along the circle around the beam axis [1,19]. The sign of l is relative to the handedness of helical phase front. The positive is for left helical phase front and negative is for right helical phase front (from the point of view of the receiver). In principle, l can take an arbitrary integer number ranged from $-\infty$ to $+\infty$, therefore, the state of OAM-carrying mode is infinite. Figure 1 shows the helical phase fronts of $l = 0$, 1, -1 and 2. Meanwhile, the OAM is the component of angular momentum of a light beam that is only dependent on the spatial field distribution but not on the polarization. Thus, the OAM mode can be classified into two types according to the state of polarization (SOP) that the beam carries. One type is the linearly-polarized OAM (LP-OAM) whose polarization states of every point on the mode cross-section are the linear polarization. This kind of OAM mode has no SAM. The other type is circularly-polarized OAM (CP-OAM) whose polarization states of every point on the mode cross-section are the circular polarization.

In the free-space system, the OAM beams can be generated via numerous methods such as spatial light modulators [20], computer-generated fork holograms [21], spiral phase plates [22], cylindrical lens pairs [23], q-plates [24], etc. Although those spatial generation methods have the advantages of strong scalability and low crosstalk, there are two common defections for them, i.e., high insertion loss and large volume.

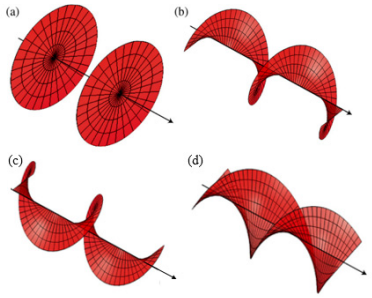

Figure 1. Helical phase fronts for (**a**) $l = 0$, (**b**) $l = 1$, (**c**) $l = -1$, and (**d**) $l = 2$. Reprinted with permission from [19], Copyright 2011 The Optical Society of America.

Compared with free-space generation systems, fiber-based methods have the advantage of the low insertion loss. Moreover, the devices in fiber-based generation methods are smaller, which greatly facilitates miniaturization. In the fiber, the $OAM_{\pm l}$ modes can be obtained by combining the two sets of fiber mode bases, LP mode and vector mode bases. The LP mode bases (LP_{lmax}, LP_{lmay}, LP_{lmbx} and LP_{lmby}) and vector mode bases ($HE^{e/o}$, $EH^{e/o}$, TE and TM) are respectively scalar and vector solutions to Maxwell Equation in the fiber [25]. Here, "e" and "o" refer to the even and odd modes, "m" is the radial order, denoting the number of radial nodes of the mode and l is the azimuthal order. The l order LP mode bases can be expressed by the Equation (1).

$$\begin{aligned} LP_{lmax} &= \vec{x}F_{lm}(r)\cos(l\theta) LP_{lmay} = \vec{y}F_{lm}(r)\cos(l\theta) \\ LP_{lmbx} &= \vec{x}F_{lm}(r)\sin(l\theta) LP_{lmby} = \vec{y}F_{lm}(r)\sin(l\theta) \end{aligned} \tag{1}$$

where $\vec{x}$ and $\vec{y}$ denote the linear polarization along the x-axis and y-axis, respectively; $F_{lm}(r)$ represents the radial field distribution and θ is the azimuthal coordinate. The vector mode bases have the following transverse electric field distributions:

$$\begin{aligned} \begin{Bmatrix} HE^{e}_{l+1,m} \\ HE^{o}_{l+1,m} \end{Bmatrix} &= F_{l,m}(r)\begin{Bmatrix} \vec{x}\cos(l\theta) - \vec{y}\sin(l\theta) \\ \vec{x}\sin(l\theta) + \vec{y}\cos(l\theta) \end{Bmatrix} \quad (l \geq 1) \\ \begin{Bmatrix} EH^{e}_{l-1,m} \\ EH^{o}_{l-1,m} \end{Bmatrix} &= F_{l,m}(r)\begin{Bmatrix} \vec{x}\cos(l\theta) + \vec{y}\sin(l\theta) \\ \vec{x}\sin(l\theta) - \vec{y}\cos(l\theta) \end{Bmatrix} \quad (l > 1) \\ \begin{Bmatrix} TM_{0,m} \\ TE_{0,m} \end{Bmatrix} &= F_{l,m}(r)\begin{Bmatrix} \vec{x}\cos(\theta) + \vec{y}\sin(\theta) \\ \vec{x}\sin(\theta) - \vec{y}\cos(\theta) \end{Bmatrix} \quad (l = 1) \end{aligned} \tag{2}$$

When two LP modes owning the same polarization directions are combined with a $\pm\pi/2$ phase shift, the LP-OAM mode with same polarization as the LP modes is generated [26], as shown in Equation (3); When the even and odd modes of same vector mode (HE or EH) are combined with $\pm\pi/2$ phase shift, the superimposed mode is CP-OAM mode, as shown in Equation (4). The OAM handedness and SAM handedness of modes based on the HE bases are the same, while those of modes based on the EH bases are opposite [25].

$$\begin{Bmatrix} LP_{lmax} \pm iLP_{lmbx} \\ LP_{lmay} \pm iLP_{lmby} \end{Bmatrix} = F_{lm}(r)\begin{Bmatrix} \vec{x}OAM_{\pm l,m} \\ \vec{y}OAM_{\pm l,m} \end{Bmatrix} \tag{3}$$

$$\begin{Bmatrix} HE^{e}_{l+1,m} \pm iHE^{o}_{l+1,m} & (l > 1) \\ EH^{e}_{l-1,m} \pm iEH^{o}_{l-1,m} & (l > 1) \end{Bmatrix} \text{or} \begin{Bmatrix} HE^{e}_{l+1,m} \pm iHE^{o}_{l+1,m} & (l = 1) \\ EH^{e}_{l-1,m} \pm iEH^{o}_{l-1,m} & (l = 1) \end{Bmatrix} = F_{l,m}(r)\begin{Bmatrix} \sigma^{\pm}OAM_{\pm l,m} & (l \geq 1) \\ \sigma^{\mp}OAM_{\pm l,m} & (l \geq 1) \end{Bmatrix} \tag{4}$$

3. Three Kinds of Tunable OAM Modes

3.1. The OAM Varies from −l to l with Homogeneous State of Polarization (SOP) along the Longitude of Orbital Poincaré Sphere (PS)

The mode with OAM from $-l$ to l and homogeneous SOP can be produced by overlapping two collinear classical OAM modes with variable relative amplitudes and equal but opposite phase chirality [16]. This kind of tunable OAM mode could maintain a constant geometry and total intensity during tuning, which is valuable for some applications such as the vortex tweezers and optical manipulation [2–5,17,18]. It is worth noting that the polarizations of two collinear classical OAM modes are the same. The superimposed mode is described by the equation:

$$\psi_1 = a_1|\mathrm{N}_l\rangle + b_1 \mathrm{e}^{i\varphi_1}|\mathrm{S}_l\rangle \tag{5}$$

with positive, real amplitudes a_1, b_1 and relative phase ϕ_1. In addition, the squares of amplitudes add up to unity. N_l and S_l are the two OAM modes owning topological charge $-l$ and $+l$ with the same polarization, respectively.

$$\begin{aligned} |\mathrm{N}_l\rangle &= \mathrm{e}^{-il\theta}(\mathrm{E_x}\vec{\mathrm{x}} + \mathrm{E_y}\vec{\mathrm{y}})/\sqrt{(|\mathrm{E_x}|_2 + |\mathrm{E_y}|_2)} \\ |\mathrm{S}_l\rangle &= \mathrm{e}^{+il\theta}(\mathrm{E_x}\vec{\mathrm{x}} + \mathrm{E_y}\vec{\mathrm{y}})/\sqrt{(|\mathrm{E_x}|_2 + |\mathrm{E_y}|_2)} \end{aligned} \tag{6}$$

where $\mathrm{E_x}$ and $\mathrm{E_y}$ are the complex amplitudes of x and y polarizations, respectively. In agreement with intuitive arguments, the amplitudes a_1 and b_1 govern the relative contribution of $\mathrm{OAM}_{+\ell}$ and $\mathrm{OAM}_{-\ell}$ to the local and total orbital angular momentum. In general, the average OAM value that mode carries is calculated from the power in each OAM mode, as shown in Equation (7). The P_l represents the power in each OAM mode [27].

$$\mathrm{L_{ave}} = \frac{\sum lP_l}{\sum P_l} = \frac{l \times |a|^2 + (-l) \times |b|^2}{|a|^2 + |b|^2} \tag{7}$$

In 1999, M. J. Padgett and J. Courtial proposed an orbital PS to represent this kind of tunable OAM mode intuitively [28]. The north and south poles of the orbital PS represent the OAM modes with equal ℓ value but opposite helicity, respectively. Similar to the polarization PS [29], all the points on the orbital PS can be described as the superposition of the two poles. Therefore, according to Equation (5), the orbital PS can be used to describe completely all the states for this kind of tunable OAM. Figure 2a,b show the mode patterns, phase distributions and polarization states on the two orbital PSs when $l = 1$ and $l = 4$, respectively.

Unlike the classical OAM mode, the amplitude and phase of the superimposed mode vary with azimuthal coordinate, which can be changed by modulating the relative amplitudes of OAM_{+l} and $\mathrm{OAM}_{-\ell}$ modes. When a = 0 or b = 0, the superimposed mode has the phase of a classical OAM_{+l} or $\mathrm{OAM}_{-\ell}$ mode which lies on the south or north pole, as the S_l and N_l points shown in Figure 2a,b; When a = b, the phase of the mode is binary with $2l$ alternating phase segments of 0 and π, which is equivalent to the phase of the optical cogwheel. This mode carries no orbital angular momentum and possesses $2l$ intensity peaks about the azimuthal coordinate, which is the $\mathrm{LP}_{\ell\mathrm{m}}$ mode of fiber and lies on the equator. The intensity fringes will occur to rotate about the center of the resultant beam by adjusting the relative phase (ϕ_1) of the two overlapping modes. We show the mode patterns of two points (H_l and V_l) which are located at the start and end points of the diameter on the equator. The H_l and V_l points are the combination mode of two poles owning same amplitude with $\phi_1 = 0$ and π, respectively.

$$|\mathrm{H}_l\rangle = \frac{|\mathrm{N}_l\rangle + |\mathrm{S}_l\rangle}{\sqrt{2(|\mathrm{E_x}|_2+|\mathrm{E_y}|_2)}} = \frac{\sqrt{2}[\cos(l\theta)((\mathrm{E_x}\vec{\mathrm{x}} + \mathrm{E_y}\vec{\mathrm{y}})]}{\sqrt{(|\mathrm{E_x}|_2+|\mathrm{E_y}|_2)}}$$
$$|\mathrm{V}_l\rangle = -i\frac{|\mathrm{N}_l\rangle - |\mathrm{S}_l\rangle}{\sqrt{2(|\mathrm{E_x}|_2+|\mathrm{E_y}|_2)}} = \frac{-\sqrt{2}[\sin(l\theta)((\mathrm{E_x}\vec{\mathrm{x}} + \mathrm{E_y}\vec{\mathrm{y}})]}{\sqrt{(|\mathrm{E_x}|_2+|\mathrm{E_y}|_2)}} \quad (8)$$

When $0 < |a_1 - b_1| < 1$, the local curvature of the helical wavefront is no longer constant nor linear. However, the phase singularity remains, qualifying the beam as a kind of optical vortex. Meanwhile, the intensity distribution also becomes an intermediate state between the LP mode and OAM mode. For $0 < a_1 - b_1 < 1$, the superimposed mode has the negative average OAM value and hence lies on the upper hemisphere. For $-1 < a_1 - b_1 < 0$, the superimposed mode has the positive average OAM value and lies on the lower hemisphere. The A_l and B_l show two specific points on the upper and lower hemisphere, respectively. Therefore, when the relative amplitude $(a_1 - b_1)$ varies from −1 to 1, the superimposed mode will change along the longitude and the average OAM value will also vary from l to $-l$.

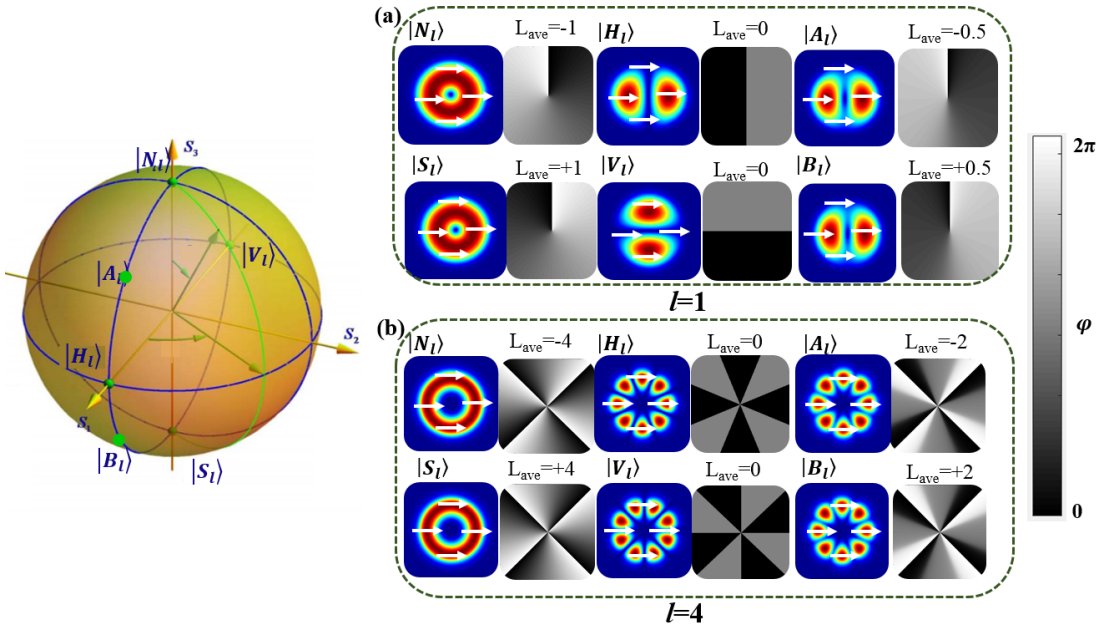

Figure 2. (**a**) Intensity profiles, polarization states and the phase distributions of superimposed mode when $l = 1$ and (**b**) $l = 4$. The north pole N_l and south pole S_l represent orthogonal circularly polarized modes with topological charges of $-l$ and $+l$; The points H_l and V_l represent the two points on the equator; The A_l and B_l points of (**a**) represent the two modes with average orbital angular momentum (OAM) values of −0.5 and 0.5 for $l = 1$. The A_l and B_l points of (**b**) represent the two modes with average OAM values of −2 and 2 for $l = 4$.

3.2. The OAM Varies from −l to l with Inhomogeneous SOP Along the Longitude of Higher-Order PS

The above tunable OAM modes have conventional homogeneous polarizations. In other words, the SOP of each point in the mode is same and invariant along the azimuthal coordinate. Recently there has been increasing interest in the modes with inhomogeneous SOPs. For those vector vortex (VV) modes, each point of the electrical field is the same polarization (linear, elliptical and circular polarization), but the polarized direction of each point is related to the azimuthal coordinate, such as the radial and azimuthal polarized cylindrical vector (CV) beams [30]. The VV modes extend the properties of conventional homogeneous polarization, such as the ability to produce strong longitudinal field

components and smaller waist sizes upon focusing by high numerical aperture objectives, which may have important applications in nanoscale optical imaging and manipulation [31–35].

A higher-order PS is introduced as the theoretical framework for describing the spatially inhomogeneous SOPs of generalized vortex modes [36,37], as shown in Figure 3. Similar to the points on the orbital PS, arbitrary ones on the higher-order PS can be obtained by the linear combination of the modes on the two poles. The two poles are orthogonal CP-OAM modes with opposite topological charge.

$$\psi_2 = a_2\left|\mathrm{N}_l^{\mathrm{R}}\right\rangle + b_2 \mathrm{e}^{i\varphi_2}\left|\mathrm{S}_l^{\mathrm{L}}\right\rangle \tag{9}$$

where

$$\left|\mathrm{N}_l^{\mathrm{R}}\right\rangle = \mathrm{e}^{-il\theta}(\vec{\mathrm{x}} + i\vec{\mathrm{y}})/\sqrt{2} \tag{10}$$

$$\left|\mathrm{S}_l^{\mathrm{L}}\right\rangle = \mathrm{e}^{+il\theta}(\vec{\mathrm{x}} - i\vec{\mathrm{y}})/\sqrt{2} \tag{11}$$

Equations (10) and (11) represent right and left circularly-polarized OAM modes with topological charge $-l$ and $+l$, respectively. The coefficients a_2 and b_2 are the amplitudes of the Equations (10) and (11), respectively, and the ϕ_2 is the relative phase between them. The higher-order PS has five salient features: (1) For $l > 1$, the OAM and SAM handedness of each pole can be the same or opposite, therefore two spheres are needed to describe higher-order SOPs of VV modes. (2) All the modes on the PS have annular intensity profiles and a dark hollow center, which possess phase or polarization singularities. (3) The modes can degenerate to the modes on the orbital PS through a linear polarizer, e.g., horizontally orientated as depicted by the double-sided arrows in the Figure 3a,b. (4) When the state of mode changes along the longitude, the average OAM value varies from $-l$ to l and the SAM changes from -1 to 1 (1 to -1), correspondingly. Figure 3a,b show intensity profiles, polarization states and phase distributions of six points on the two higher-order PSs with $l = \pm 1$, respectively. For $l = +1$, the handedness of OAM and SAM on each pole is opposite, as $\mathrm{N}_l^{\mathrm{R}}$ and $\mathrm{S}_l^{\mathrm{L}}$ show in Figure 3a. This higher-order PS can completely characterize a general cylindrical vector mode [38], such as radial and azimuthal polarization, which are equivalent to TE and TM fiber modes. The H_l and V_l points are the TE_{01} and TM_{01} fiber modes which are obtained by the combination mode of two poles owning same amplitudes with $\phi_2 = 0$ and π, respectively. The deduction processes about H_l and V_l points are described by Equation (12). In addition, we choose two specific points (A_l and B_l) to illustrate the intensity and polarization distributions on the upper and lower hemisphere with -0.5 and 0.5 average OAM values, respectively.

$$\begin{aligned} |\mathrm{H}_l\rangle &= \frac{\left|\mathrm{N}_l^{\mathrm{R}}\right\rangle + \left|\mathrm{S}_l^{\mathrm{L}}\right\rangle}{2} = \cos(l\theta)\vec{\mathrm{x}} + \sin(l\theta)\vec{\mathrm{y}} \\ |\mathrm{V}_l\rangle &= -i\frac{\left|\mathrm{N}_l^{\mathrm{R}}\right\rangle - \left|\mathrm{S}_l^{L}\right\rangle}{2} = -\sin(l\theta)\vec{\mathrm{x}} + \cos(l\theta)\vec{\mathrm{y}} \end{aligned} \tag{12}$$

For $l = -1$, the handedness of OAM and that of SAM on each pole are the same, shown in the Figure 3b. Similarly, $\mathrm{N}_l^{\mathrm{R}}$ and $\mathrm{S}_l^{\mathrm{L}}$ represent the modes on the north and south poles. This higher-order PS can describe the so-called π-vector modes [39] which are equivalent to the $\mathrm{HE}_{21}^{\mathrm{e}}$ and $\mathrm{HE}_{21}^{\mathrm{o}}$ fiber modes. H_l and V_l are the two points on the equator, whose average OAM values are both 0. Intermediate modes between the pole and equator have the elliptical polarizations and annular intensity profiles. The A_l and B_l are, respectively, the points with -0.5 and 0.5 average OAM values.

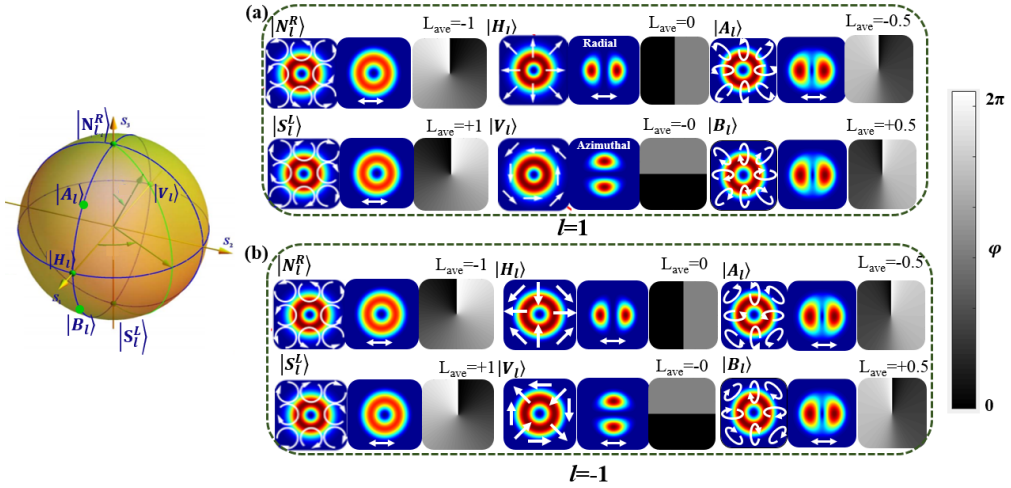

Figure 3. (**a**) Intensity profiles, polarization states and phase distributions of superimposed modes when $l = 1$ and (**b**) $l = -1$. The north pole N_l^R and south pole S_l^L represent orthogonal circularly-polarized modes with topological charges of $-l$ and $+l$; The points H_l and V_l represent the two points on the equator; The A_l and B_l points represent the two modes with −0.5 and 0.5 average OAM values, respectively.

3.3. The OAM Varies from l to n with Inhomogeneous SOP Along the Longitude of Hybrid-Order PS

For the second kind of tunable OAM mode, the polarization states and OAMs of modes on the higher-order PS are still confined to some special cases. For example, the modes on the equator have the azimuthally and radially linear polarization, but they are only the single vector beams possessing spatially inhomogeneous SOP and carrying zero-order OAM. The OAM modes on the poles of higher-order PS are only the single vortex beams with spiral wavefronts. Compared to a single vector mode and a single vortex mode, a vector vortex mode provides more degrees of freedom in optical manipulation [40,41]. Hence, in 2015, the hybrid-order PS is proposed to describe the evolution of the OAM and SOP, which extends the orbital PS and higher-order PS to a more general form [42].

The representation of the modes on the hybrid-order PS is the same as those on the higher-order PS except the orbital states on the poles. The orbital states of the two poles on orbital and higher-order PSs have the same value but opposite signs. Unlike the previous PSs, the orbital states of the poles on the hybrid-order PS are not confined to the same order topological charge and can be chosen arbitrarily. Any one mode on the hybrid-order PS can be expressed as the superposition of two poles:

$$\psi_3 = a_3\left|\mathrm{N}_l^{\mathrm{R}}\right\rangle + b_3 e^{i\varphi_3}\left|\mathrm{S}_n^{\mathrm{L}}\right\rangle \tag{13}$$

$$\left|\mathrm{N}_l^{\mathrm{R}}\right\rangle = e^{il\theta}(\vec{\mathrm{x}} + i\vec{\mathrm{y}})/\sqrt{2} \tag{14}$$

$$\left|\mathrm{S}_n^{\mathrm{L}}\right\rangle = e^{in\theta}(\vec{\mathrm{x}} - i\vec{\mathrm{y}})/\sqrt{2} \tag{15}$$

Equations (14) and (15) represent right and left circularly-polarized modes with different topological charges l and n, respectively. Any mode on the hybrid-order PS can be achieved by changing the coefficients a_3 and $b_3 e^{i\varphi_3}$. Generally, the equatorial points on the hybrid-order PS represent the superposition of the two poles with equal intensities. The $H_{l,n}$ and $V_{l,n}$ of Figure 4 are the two equatorial points when $\phi_3 = 0$ and π, respectively.

$$\begin{aligned}\left|\mathrm{H}_{l,n}\right\rangle &= \frac{\left|\mathrm{N}_l^{\mathrm{L}}\right\rangle + \left|\mathrm{S}_n^{\mathrm{L}}\right\rangle}{2} = \exp\frac{i(l+n)\theta}{2}\left[\cos\frac{(l-n)\theta}{2}\vec{\mathrm{x}} + \sin\frac{(l-n)\theta}{2}\vec{\mathrm{y}}\right] \\ \left|\mathrm{V}_{l,n}\right\rangle &= -i\frac{\left|\mathrm{N}_l^{\mathrm{L}}\right\rangle - \left|\mathrm{S}_n^{\mathrm{L}}\right\rangle}{2} = \exp\frac{i(l+n)\theta}{2}\left[\cos\left(\frac{l-n}{2}\theta + \frac{\pi}{2}\right)\vec{\mathrm{x}} + \sin\left(\frac{l-n}{2}\theta + \frac{\pi}{2}\right)\vec{\mathrm{y}}\right]\end{aligned} \tag{16}$$

From Equation (16), it should be noted that the equatorial points represent modes carrying $(l + n)/2$ per photon. The relative phase of the superposition determines the orientation of the longitude.

Figure 4 depicts a hybrid-order PS at the situation of the north pole with state $\sigma = +1$ and $l = 0$, while the south pole with $\sigma = -1$ and $n = +2$. The N_l^R and S_n^L separately represent north and south poles; The $H_{l,n}$ and $V_{l,n}$ indicate two points on the equator. The $A_{l,n}$ and $B_{l,n}$ denote two points on the upper and lower hemispheres with 0.5 and 1.5 average OAM values. The average OAM that modes carry will change from l to $(l + n)/2$ and then to n along the longitude on the hybrid-order PS.

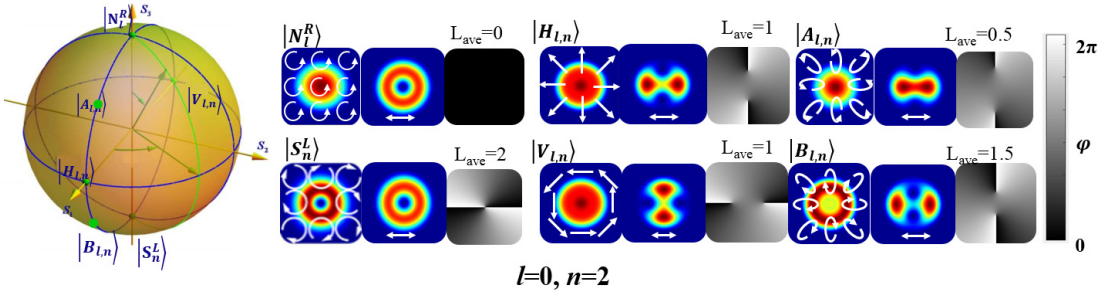

Figure 4. Intensity profiles, polarization states and phase distributions of superimposed modes when $\ell = 1$ and $n = 2$. The north pole N_l^R and south pole S_n^L represent orthogonal circularly-polarized modes with topological charges of l and n; The points $H_{l,n}$ and $V_{l,n}$ represent the two points on the equator; The $A_{l,n}$ and $B_{l,n}$ points represent the two modes with 0.5 and 1.5 average OAM values, respectively.

3.4. The Relationship Among the Three Kinds of Tunable OAM Modes

According to the representations of three kinds of tunable OAM modes, we find that there is a progressive relationship from orbital PS to higher-order PS, then to hybrid PS. Figure 5 shows the intuitive sketch describing the phase and polarization distributions of north and south poles on the three PSs. The white arrows represent polarization states and black-and-white images represent phase distributions. From the orbital PS to higher-order PS, the SOPs on the two poles vary from the same polarization to orthogonal circularly-polarized polarization. From the higher-order PS to hybrid-order PS, the SOPs on the two poles are kept while the orbital states vary from same order to different orders.

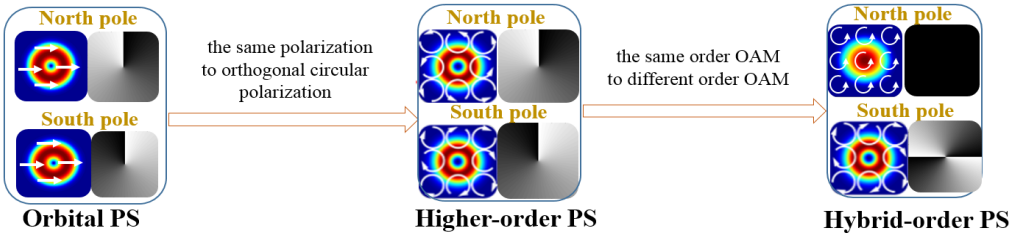

Figure 5. Sketch of the progressive relationship from the orbital Poincaré sphere (PS) to higher-order PS, then to hybrid-order PS.

4. Methods for Generation of Tunable OAM

The three kinds of tunable OAM modes can be considered as not only the superposition of classical OAM modes physically, but also the combination of x and y polarizations with spatially-variant amplitude and phase mathematically. Thus, the modes can be realized by some free-spatially optical elements that change the polarization of each point on the cross section of mode. Equations (17)–(19) show purely mathematical expressions in the form of Jones vectors, where the first and second elements of the vectors represent components of the field along the horizontal (x) and vertical (y) axes. The $A(\theta)$, $B(\theta)$, $\varphi_x(\theta)$ and $\varphi_y(\theta)$ represent the spatially-variant amplitude and phase factors, respectively.

$$\text{Orbital PS}: \begin{bmatrix} E_x(a_1 e^{-il\theta} + b_1 e^{i\varphi_1} e^{+il\theta}) \\ E_y(a_1 e^{-il\theta} + b_1 e^{i\varphi_1} e^{+il\theta}) \end{bmatrix} = \begin{bmatrix} E_x(A(\theta) e^{i\varphi_x(\theta)}) \\ E_y(B(\theta) e^{i\varphi_y(\theta)}) \end{bmatrix} \quad (17)$$

$$\text{Higher} - \text{order PS}: \begin{bmatrix} (a_2 e^{-il\theta} + b_2 e^{i\varphi_2} e^{+il\theta}) \\ i(a_2 e^{-il\theta} - b_2 e^{i\varphi_2} e^{+il\theta}) \end{bmatrix} = \begin{bmatrix} A(\theta) e^{i\varphi_x(\theta)} \\ B(\theta) e^{i\varphi_y(\theta)} \end{bmatrix} \tag{18}$$

$$\text{Hybrid} - \text{order PS}: e^{i\frac{(l+n)}{2}\theta} \begin{bmatrix} (a_3 e^{i\frac{(l-n)}{2}\theta} + b_3 e^{i\varphi_3} e^{-i\frac{(l-n)}{2}\theta}) \\ i(a_3 e^{i\frac{(l-n)}{2}\theta} - b_3 e^{i\varphi_3} e^{-i\frac{(l-n)}{2}\theta}) \end{bmatrix} = e^{i\frac{(l+n)}{2}\theta} \begin{bmatrix} A(\theta) e^{i\varphi_x(\theta)} \\ B(\theta) e^{i\varphi_y(\theta)} \end{bmatrix} \tag{19}$$

4.1. Free Space Method for Generation of Tunable OAM

Free-space generation methods of tunable OAM modes are generally assisted by spatial light modulators (SLMs) [17,43–51], deformable mirrors (DMs) [51], q-plate cells [52–55] and metasurfaces [56], and spiral phase plates (SPPs) [22]. Those optical elements can change the phase distribution of a mode, where the SLM and DM are programmable and can control the phase dynamically. In addition, the DM and SPP are polarization insensitive.

SLM is a computer-addressable reflective liquid crystal (LC) display which can impose any desired phase profile onto an incoming collimated beam by controlling the voltage (V) of each SLM pixel [46]. The phase retardation for each SLM pixel can be described as a function of the voltage (V) applied: $\delta(V) = (2\pi/\lambda)(n_e(V) - n_o)d$, where d is the thickness of the LC layer, n_e and n_o are the extraordinary and ordinary refractive indices of the LC retarder, respectively. Because of the birefringent nature of LC, when the input polarization state makes a projection on both the fast and slow axes of the SLM, the polarization state can be altered. The polarization property of the SLM can be exploited by the appropriate optical setup to achieve the desired change in the polarization. Moreover, the combination of the SLM and wave plates can be used to control the amplitudes of x and y polarizations due to the birefringent nature. For the SLM, it has the advantage of high flexibility due to the arbitrarily adjustable phase distribution, but also has the disadvantages of maximum power density limitation and large loss.

The DM is composed of many units. Each unit has its own independent controller. Under the control of external voltage, it can transform the wavefront phase [51]. In principle, the SLM modulates the wave-front phase by controlling the refractive index, and the DM modulates the wave-front by changing the distance of light propagation. As a phase controller, the DM is energy efficient and highly flexible, while the range of controllable phase is limited.

The q-plate cell is essentially birefringent waveplates with a uniform birefringent phase retardation δ across the plate thickness (which can be electrically controlled) and a space-variant transverse optical axis distribution exhibiting a topological charge "2q" [52]. The charge "q" represents the number of rotations of the local optical axis in a path circling once around the center of the plate. When the q-plate cell is illuminated by a circularly-polarized vortex beam, the output beam from the q-plate cell is the combination of two different-order OAM modes with adjustable amplitudes. For the q-plate usually used, it is a q-plate cell with a uniform birefringent phase retardation $\delta = \pi$. If a Gaussian mode with arbitrary polarization passes through the q-plate, the output mode will perform the following linear transformation, as shown in Equation (20) [54], where σ^+ and σ^- respectively indicate the left and right circular polarization. Thus, a q-plate cell can convert a Gauss beam to a vector beam and generate a vortex phase in one step. However, the "q" value is fixed, so the flexibility is poor.

$$q \cdot (A\sigma^+ + B\sigma^-) = A\sigma^- e^{i2q\theta} + B\sigma^+ e^{-i2q\theta} \tag{20}$$

The metasurface with tailorable structure geometry, as a two-dimensional electromagnetic nanostructure, possesses unparalleled advantages in optical phase and polarization manipulation, especially in subwavelength scale [57]. The operation principle is the same as the q-plate. But it is the difficult to fabricate and untunable once fabricated.

Free-space generation methods can be classified into three types according to the controllable variables. Figures 6–8 simply show schematic diagrams used to generate the tunable OAM mode

based on the free-space system. The components marked by red and gray frames in Figures 6–8 are the adjusted ones and fixed ones, respectively.

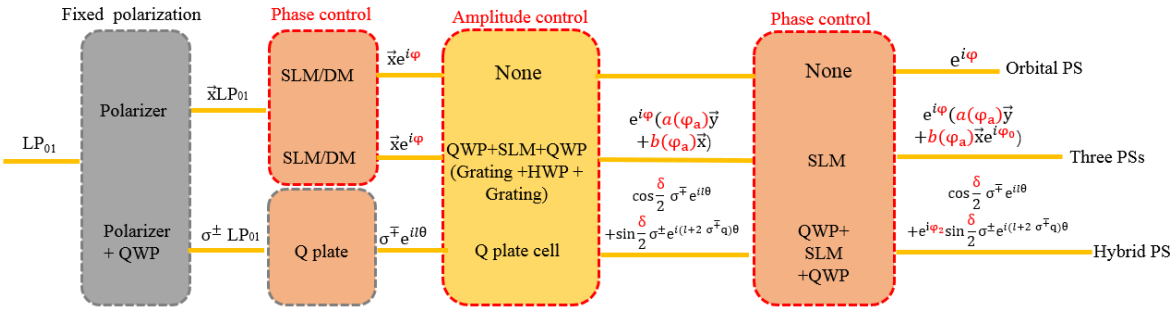

Figure 6. The flow chart of tunable OAM generation by adjusting the phase distributions on the spatial light modulators (SLMs), deformable mirrors (DMs) and q-plate cells.

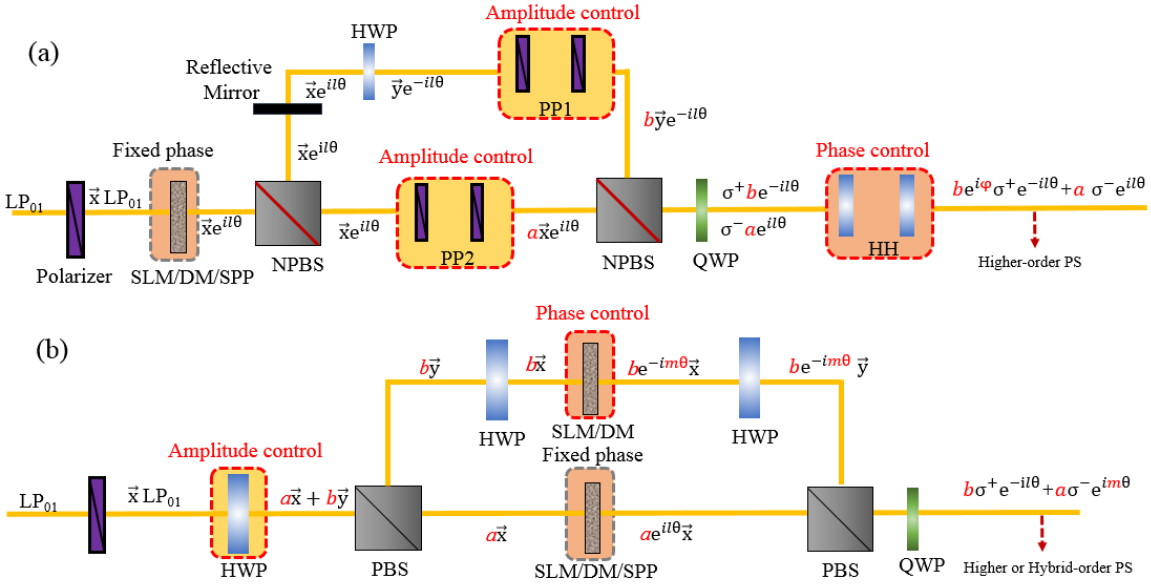

Figure 7. The flow chart of tunable OAM generation by interfering with two Laguerre-Gaussian modes. Adjusting phase and amplitude factors of two branches by (**a**) optical elements and (**b**) a HWP and a SLM.

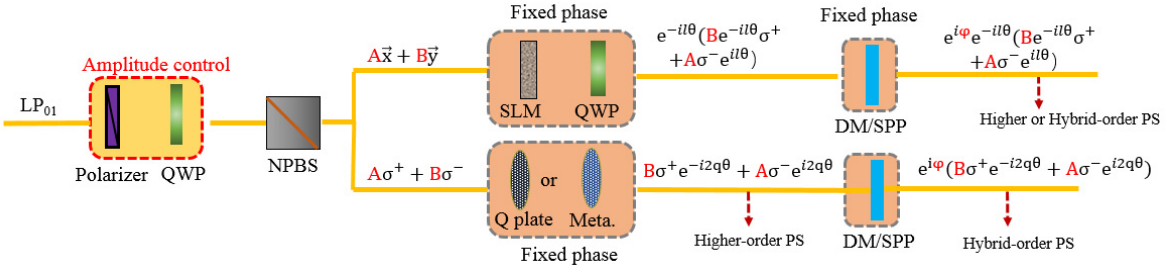

Figure 8. The flow chart of tunable OAM generation by continuously changing the state of input polarization.

The first kind of generation method is shown in Figure 6, which obtains tunable OAM modes by changing the phase information imposed on the SLMs, DMs or q-plate cells. When a Gaussian beam with linear polarization is launched to a programmable phase element (SLM or DM), the topological charge can be tuned by electrically changing the phase information loaded on them, which can obtain the modes on the orbital PS, as shown the first row in Figure 6 [17,43–46,52]. The second row of Figure 6b shows 3 sections as subsystems to control respectively three degrees of freedom in the optical

field, e.g., the phase, amplitude and retardation between the x and y components [47,48]. The section of amplitude is achieved by the combination of two quarter-wave plates (QWPs) and a SLM [46] or the combination of a half-wave plate (HWP) and two diffraction gratings [47]. In ref. [46], the fast axes of the QWPs are along 45° and 135° with respect to the horizontal axis, respectively. By loading appropriate phase information on the three sections, this system can generate arbitrary modes on the three PSs. The modes on the three PSs can be obtained when the mathematical expression of the output mode equals to the one of Equations (17)–(19). When a Gaussian beam with circularly polarization is launched to two q-plate cells and a SLM, two different-order classical OAM modes with orthogonally-circular polarization are generated. The amplitude and phase of two OAM modes can be adjusted by changing the retardations of the q-plate cells and the SLM [52], which can go through all the points on the hybrid PS, as shown in the third row of Figure 6.

For these kinds of generation method, the greatest advantage is high flexibility due to the phase distributions and retardations can be arbitrarily electrically controlled. However, the common shortcoming is limited response speed.

For the second type, the tunable OAM modes can be generated by interfering two Laguerre–Gaussian modes with same or different topological charges, as shown in Figure 7. The modulation of amplitude is realized by rotating the optical elements [49,50], where "*a*" and "*b*" are the amplitudes of x and y polarizations. The modulation of phase between two Laguerre–Gaussian modes can be realized by rotating the optical elements [48] or changing the phase distribution of SLM/DM [49]. Because the phase difference between the two split and recombined beams determines the properties of the generated vector beams, this kind of method employing interferometry may be vulnerable to environmental noise like vibrations or air circulation. Another weakness is the slow rotating speed for the optical elements.

The third type of generating the beam with tunable OAM in the free-space system is achieved by continuously changing the state of input polarization [51,55–59], as shown in Figure 8. A Gaussian beam with arbitrary polarization state can be generated by using a polarizer followed by an arbitrarily oriented QWP. The arbitrary polarization state can be expressed as the $A\vec{x} + B\vec{y}$ in the basis of x and y polarizations or $A\sigma^{+} + B\sigma^{-}$ in the basis of right- and left-hand circular polarizations, where the symbols "A" and "B" are complex amplitudes.

When a Gaussian mode with arbitrary polarization is injected to the combination of a SLM, a SPP/DM and a QWP, the SLM is used to generate the helical phase distributions of x and y polarizations. The SPP/DM is for compensating superfluous phase factor, and the QWP can convert the orthogonal linear polarizations to orthogonal circular polarizations. As shown in the top branch of Figure 8, when $\varphi = l\theta$, the modes on the higher-order PS can be generated by adjusting the input polarization [50]. When $\varphi = m\theta$, where $m \neq l$, the system can generate the modes on the hybrid-order PS. If the input beam is launched to a q-plate, the output mode will be located on higher-order PS according to Equation (20), as shown in the bottom branch of Figure 8 [53–57]. In addition, by adding a phase factor $\exp(i(l + n)\theta/2)$ into the bottom branch of Figure 8, the tunable OAM on the hybrid-order PS can also be generated by adjusting the input polarization [52,55]. The extra phase can be achieved by numerous methods, such as spiral phase plates, SLM, diffractive elements and fork gratings.

This kind of generation methods involve fewer components. The speed of adjusting polarization is very fast, which leads to a rapid conversion between modes on the PS.

We conclude the spatial generation methods, as shown in Table 1. The table lists the adjustable variations, devices and the types of tunable OAM modes.

Table 1. The free-space generation methods.

Adjustable Variation	Reference	Device	The Type of Tunable OAM
Phase distribution	[17,42–45]	SLM	Orbital PS
	[46,47]	SLM + QWP	Three PSs
	[51]	DMs	Orbital PS
	[52]	Q-plate	Hybrid-order PS
Interference	[48,49]	SLM	Higher- or Hybrid-order PS
Input polarization	[50]	SLM + QWP	Higher-order PS
	[52–55]	Q plate + SPP	Higher- or Hybrid-order PS
	[56]	Metasurface	Higher-order PS

4.2. The Fiber-Based Generation of Tunable OAM

For the fiber-based devices, the methods for tunable OAM mode generation can be classified into three types according to the adjusting schemes. Figure 9 simply shows schematic diagram usually used to generate the tunable OAM mode based on the fiber. The components marked by green arrows are the adjusted ones in the experiment.

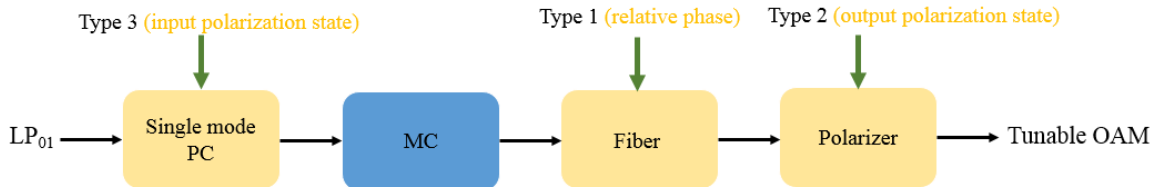

Figure 9. A typical experimental setup based on fiber to generate tunable OAM modes. PC: polarization controller, MC: mode converter.

For the first type, the tunable OAM modes can be generated by the superposition of two orthogonal LP or HE (EH) modes with tunable relative phase difference between LP (HE) modes passing through a polarizer with a fixed direction. The flow chart of the mode generation is shown in Figure 10, and the yellow parts are the variations that need to be adjusted. The tunable OAM on the orbital PS can be generated by using the first four formulas, and the tunable OAM on the higher-order PS can be generated by the last one. Firstly, the LP_{01} mode can be converted to LP_{lm} mode by many kinds of mode converters, for example, photonic lanterns [57], mode selective couplers [58] and gratings [59]. The LP_{lm} mode can be thought of as the combining result of LP_{lma} and LP_{lmb} without relative phase. The HE and EH modes can be directly generated by gratings with appropriate period [60]. When the converted two LP or HE (EH) modes pass through a length L of few-mode fiber (FMF), the relative phase between the two modes at the output of the FMF can always be written as $\Delta\delta = \frac{2\pi L \Delta neff}{\lambda}$. The Δneff represents the RI difference between two modes and λ represents the operating wavelength. Thus, in order to achieve flexible control of the relative phase between the two modes in the fiber, changing the operating wavelength λ [61,62] and the refractive index difference Δneff are two commonly used methods. So far, ways of controlling Δneff mainly depend on adjusting the pressure loaded on the fiber and rotating the paddles of few-mode polarization controller [63–65]. In addition, the LP_{11a} and LP_{11b} can be generated by respectively injecting two LP_{01} modes with slight horizontal and vertical displacement from the fiber axis and the relative phase can be controlled by using a piezo-driven delay stage [26,27,66].

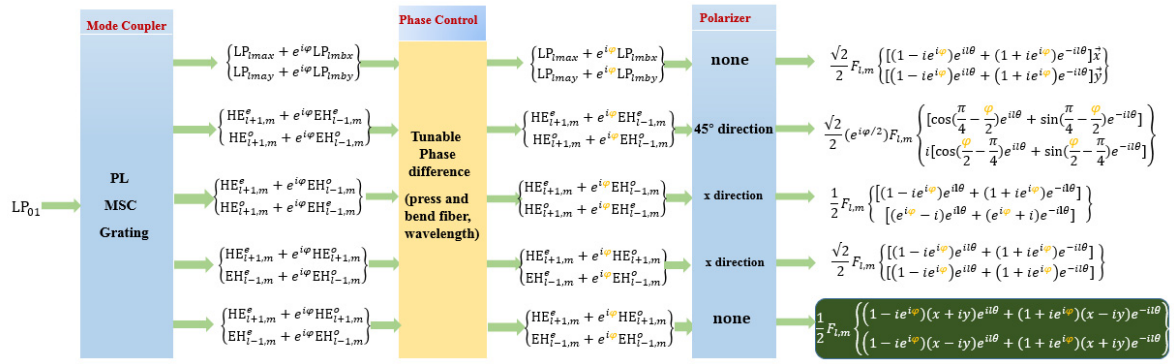

Figure 10. The flow chart of tunable OAM generation by adjusting the relative phase between two fiber modes.

The second type, the tunable OAM modes can be achieved by filtering the mixing modes which are produced by the combination of different vector modes or two spatially orthogonal LP modes owning orthogonal polarization directions with a $\pm\pi/2$ phase shift. The phase shift can be obtained in the same ways as mentioned above. Then, the continually tunable OAM can be achieved by adjusting direction of the polarizer at the output of the FMF [62,63,66,67]. The specific process is shown in Figure 11 and the "p" is the angle between the direction of the polarizer and the positive direction of the x-axis.

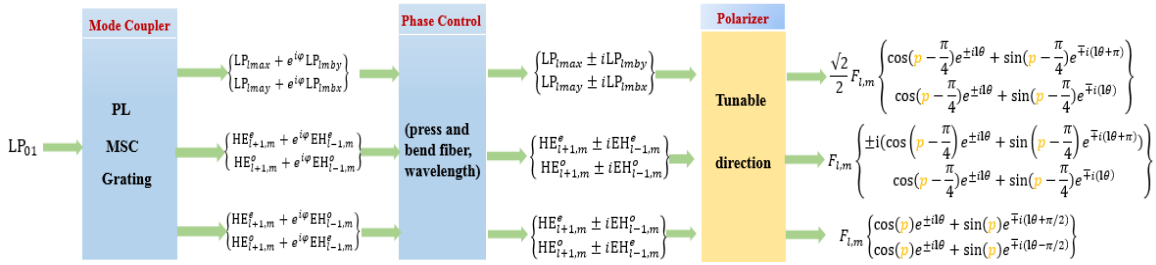

Figure 11. The flow chart of tunable OAM generation by adjusting the polarization direction.

For the third type, a method is reported to generate the beam with tunable OAM in the fiber by continuously changing the angle of linear polarization state of the input light [67], as described in Figure 12. The setup is composed of three parts, including a mode converter, a few-mode fiber that is mounted as coils in a paddle of a fiber polarization controller (PMC) and a polarizer. Considering about four linear polarization (LP) mode bases in the fiber, we deduce the transmission matrix of the first-order modes in PMC. Then, one polarization is filtered out through a polarizer. It is well known that the FMF is wound around the circumference of the PMC's paddle, and stress will induce the refractive RI difference between four orthogonal LP mode bases. If the relative phases between LP_{11ax} and LP_{11bx}, LP_{11ay} and LP_{11by} are $\pi/2$ and $-\pi/2$, the average OAM value of mode will smoothly vary from -1 to 1 with the input light polarization angle changing from 0 to π. The polarization angle (α) can be adjusted by electrical polarization controller. δ in the Figure 10 represents the relative phase between LP_{11bx} and LP_{11by}, which decides the orientation of longitude on the orbital PS.

At the end of the paper, we draw conclusions about the fiber-based generation methods, as shown in Table 2. The table lists the combination modes, adjusting variations, adjusting methods and the types of tunable OAM mode.

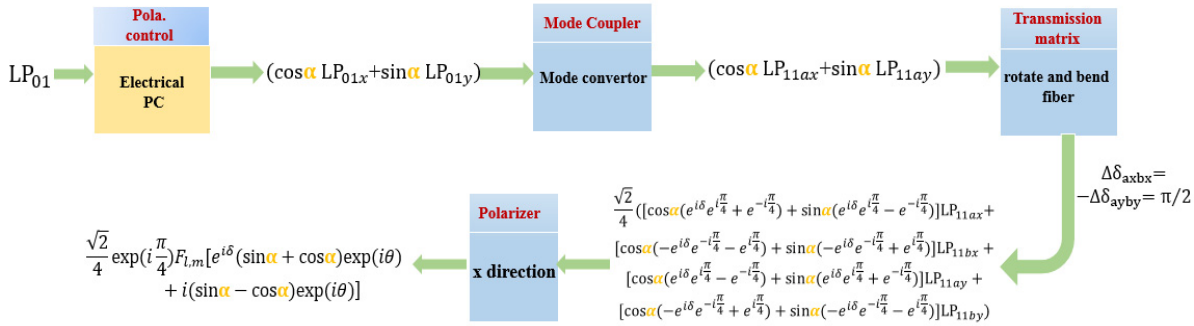

Figure 12. The flow chart of tunable OAM generation by adjusting the input polarization.

Table 2. The fiber-based generation methods.

Adjustable Variation	Reference	Combination Modes	Adjusting Method	The Type of Tunable OAM
Relative Phase (φ)	[63]	$LP_{11ax(y)}$ and $LP_{11bx(y)}$	Stress the fiber by a pair of flat slabs	Orbital PS
	[61]	$LP_{11ax(y)}$ and $LP_{11bx(y)}$	Operating wavelength λ in the PMF	Orbital PS
	[26,27]	$LP_{11ax(y)}$ and $LP_{11bx(y)}$	Piezo-driven delay stage	Orbital PS
	[62]	$HE^{e}_{2,1}$ and $TE_{0,m}$ $HE^{o}_{2,1}$ and $TM_{0,m}$ $HE^{e}_{2,1}$ and $TM_{0,m}$ $HE^{o}_{2,1}$ and $TE_{0,m}$	Wavelength λ in the ring-core fiber	Orbital PS
	[64]	$HE^{e}_{2,1}$, HE^{o}_{21}	Bend and twist RCF by paddle-type polarization controller	Orbital and higher-order PS
Polarization direction	[60,65]	$HE^{e}_{2,1}$ and $TM_{0,m}$ $TE_{0,m}$ and HE^{o}_{21}	Rotate polarizer	Orbital PS
	[62,66]	LP_{11ax} and LP_{11by} (LP_{11ax} and LP_{11by})	Rotate polarizer	Orbital PS
	[62]	$HE^{e}_{2,1}$, HE^{o}_{21} $TE_{0,m}$, $TM_{0,m}$	Rotate polarizer	Orbital PS
Input polarization	[67]	LP_{11a}	Adjust single mode PC	Orbital PS

5. Discussion and Perspective

Arbitrarily tunable OAM has excited a great diversity of interest, because of a variety of emerging applications, but its creation still remains a tremendous challenge. We review the concepts of general OAM, which extends the OAM carried by the scalar vortex modes (classical OAM mode and the modes on the orbital PS) and the OAM carried by the azimuthally varying polarized vector modes (the modes on the higher-order PS and hybrid-order PS).

In summary, due to unique characteristics, tunable OAM beams have been the subject of much interest for a variety of fundamental research studies and modern applications. There are mainly two types of methods to generate those tunable OAM beams, free-space and fiber generating methods. Each method has its own advantages and disadvantages. Free-space generating methods have advantages in terms of flexible design and easy manipulation, but active optical spatial phase modulators are expensive and may introduce additional electronic noise. Meanwhile, the volumes of spatial devices are usually large. Compared with free-space generation methods, the fiber-based generation methods have the advantages of the miniaturization and low insertion loss. However, the challenge is robustness because they are basically the combination of fibers and mode converters. The fiber is vulnerable to external influences and some methods involve alignment operation. It must be mentioned that choosing which method to generate tunable OAM modes depends more on its application scenarios. For example, for a transfer of ultrashort pulses, free-space solutions have essential advantages because of avoiding frequency chirping and pulse lengthening. For medical endoscopy, the fiber-based generation method is obviously a better way. Despite this, along with the efforts of researchers all around the world, we may see an increasing number of applications based on tunable OAM beams in the future.

Author Contributions: This paper was mainly wrote by L.F. and Y.L. and the idea originates from Y.L., S.W. and W.L. provided constructive improvements and feedback. All authors contributed to the writing and editing of the manuscript.

Funding: This paper is partly supported by National Natural Science Foundation of China (NSFC) (61875019, 61675034, 61875020, 61571067); The Fund of State Key Laboratory of IPOC (BUPT); The Fundamental Research Funds for the Central Universities.

Conflicts of Interest: The authors declare no conflict of interest.

References

1. Allen, L.; Beijersbergen, M.W.; Spreeuw, R.J.C.; Woerdman, J.P. Orbital angular-momentum of light and the transformation of Laguerre–Gaussian laser modes. *Phys. Rev. A* **1992**, *45*, 8185–8189. [CrossRef] [PubMed]
2. Padgett, M.; Bowman, R. Tweezers with a twist. *Nat. Photonics* **2011**, *5*, 343–348. [CrossRef]
3. Paterson, L. Controlled Rotation of Optically Trapped Microscopic Particles. *Science* **2001**, *292*, 912–914. [CrossRef] [PubMed]
4. Simpson, N.B.; Dholakia, K.; Allen, L.; Padgett, M.J. Mechanical equivalence of spin and orbital angular momentum of light: An optical spanner. *Opt. Lett.* **1997**, *22*, 52–54. [CrossRef] [PubMed]
5. Padgett, M.; Allen, L. Optical tweezers and spanners. *Phys. World* **1997**, *10*, 35–38. [CrossRef]
6. Molina-Terriza, G.; Torres, J.P.; Torner, L. Management of the angular momentum of light: Preparation of photons in multidimensional vector states of angular momentum. *Phys. Rev. Lett.* **2002**, *88*, 013601. [CrossRef] [PubMed]
7. Krenn, M.; Malik, M.; Erhard, M.; Zeilinger, A. Orbital angular momentum of photons and the entanglement of Laguerre–Gaussian modes. *Philos. Trans. R. Soc. A-Math. Phys. Eng. Sci.* **2017**, *375*, 20150442. [CrossRef]
8. Jack, B.; Yao, A.M.; Leach, J.; Romero, J.; Franke-Arnold, S.; Ireland, D.G.; Barnett, S.M.; Padgett, M.J. Entanglement of arbitrary superpositions of modes within two-dimensional orbital angular momentum state spaces. *Phys. Rev. A* **2010**, *81*, 043844. [CrossRef]
9. Mair, A.; Vaziri, A.; Weihs, G.; Zeilinger, A. Entanglement of Orbital Angular Momentum States of Photons. *Nature* **2001**, *412*, 313–316. [CrossRef]
10. Vaziri, A.; Weihs, G.; Zeilinger, A. Experimental Two-Photon, Three-Dimensional Entanglement for Quantum Communication. *Phys. Rev. Lett.* **2002**, *89*, 240401. [CrossRef]
11. Fürhapter, S.; Jesacher, A.; Bernet, S.; Ritsch-Marte, M. Spiral phase contrast imaging in microscopy. *Opt. Express* **2005**, *13*, 689–694. [CrossRef] [PubMed]
12. Yan, L.; Gregg, P.; Karimi, E.; Rubano, A.; Marrucci, L.; Boyd, R.; Ramachandran, S. Q-plate enabled spectrally diverse orbital-angular-momentum conversion for stimulated emission depletion microscopy. *Optica* **2015**, *2*, 900–903. [CrossRef]
13. Bernet, S.; Jesacher, A.; Severin, F.; Maurer, C.; Ritsch-Marte, M. Quantitative imaging of complex samples by spiral phase contrast microscopy. *Opt. Express* **2006**, *14*, 3792–3805. [CrossRef] [PubMed]
14. Padgett, M.J.; Allen, L. Light with a twist in its tail. *Contemp. Phys.* **2000**, *41*, 275–285. [CrossRef]
15. Wang, J. Twisted optical communications using orbital angular momentum. *Sci. China Phys. Mech. Astron.* **2019**, *62*, 034201. [CrossRef]
16. Elias, N.M. Photon orbital angular momentum in astronomy. *Astron. Astrophys.* **2008**, *492*, 883–922. [CrossRef]
17. Schmitz, C.H.J.; Uhrig, K.; Spatz, J.P.; Curtis, J.P. Tuning the orbital angular momentum in optical vortex beams. *Opt. Express* **2006**, *14*, 6604–6612. [CrossRef]
18. Gecevicius, M.; Drevinskas, R.; Beresna, M.; Kazansky, P.G. Single beam optical vortex tweezers with tunable orbital angular momentum. *Appl. Phys. Lett.* **2014**, *104*, 231110. [CrossRef]
19. Yao, A.M.; Padgett, M.J. Orbital angular momentum: Origins, behavior and applications. *Adv. Opt. Photonics* **2011**, *3*, 161–204. [CrossRef]
20. Gibson, G.; Courtial, J.; Padgett, M.J.; Vasnetsov, M.; Pas'ko, V.; Barnett, S.M.; Franke-Arnold, S. Free-space information transfer using light beams carrying orbital angular momentum. *Opt. Express* **2004**, *12*, 5448–5456. [CrossRef]
21. Heckenberg, N.R.; Mcduff, R.; Smith, C.P.; White, A.G. Generation of optical phase singularities by computer-generated holograms. *Opt. Lett.* **1992**, *17*, 221–223. [CrossRef] [PubMed]

22. Beijersbergen, M.W.; Coerwinkel, R.P.C.; Kristensen, M.; Woerdman, J.P. Helical-wavefront laser beams produced with a spiral phase plate. *Opt. Commun.* **1994**, *112*, 321–327. [CrossRef]
23. Beijersbergen, W.M.; Allen, V.D.; Veen, E.L.; Woerdman, O.H. Astigmatic laser mode converters and transfer of orbital angular momentum. *Opt. Commun.* **1993**, *96*, 123–132. [CrossRef]
24. Marrucci, L.; Karimi, E.; Slussarenko, S.; Piccirillo, B.; Santamato, E.; Nagali, E.; Sciarrino, F. Spin-to-orbital conversion of the angular momentum of light and its classical and quantum applications. *J. Opt.* **2011**, *13*, 064001. [CrossRef]
25. Ramachandran, S. Optical Vortices in Fiber. *Nanophotonics* **2013**, *2*, 455–474. [CrossRef]
26. Niederriter, R.D.; Siemens, M.E.; Gopinath, J.T. Continuously tunable orbital angular momentum generation using a polarization-maintaining fiber. *Opt. Lett.* **2016**, *41*, 3213–3216. [CrossRef]
27. Niederriter, R.D.; Siemens, M.E.; Gopinath, J.T. Simultaneous control of orbital angular momentum and beam profile in two-mode polarization-maintaining fiber. *Opt. Lett.* **2016**, *41*, 5736–5739. [CrossRef]
28. Padgett, M.J.; Courtial, J. Poincare-sphere equivalent for light beams containing orbital angular momentum. *Opt. Lett.* **1999**, *24*, 430–432. [CrossRef]
29. Kumar, A.; Ajoy, G. Poincaré Sphere Representation of Polarized Light. In *Polarization of Light with Applications in Optical Fibers*; SPIE: Bellingham WA, USA, 2011; Volume TT90, pp. 121–134.
30. Zhan, Q. Cylindrical vector beams: From mathematical concepts to, applications. *J. Syst. Sci. Complex.* **2009**, *27*, 899–910. [CrossRef]
31. Deng, D.; Guo, Q. Analytical vectorial structure of radially polarized light beams. *Opt. Lett.* **2007**, *32*, 2711–2713. [CrossRef]
32. Kozawa, Y.; Sato, S. Optical trapping of micrometer-sized dielectric particles by cylindrical vector beams. *Opt. Express* **2010**, *18*, 10828–10833. [CrossRef] [PubMed]
33. Huang, L.; Guo, H.; Li, J.; Ling, L.; Feng, B.; Li, Z. Optical trapping of gold nanoparticles by cylindrical vector beam. *Opt. Lett.* **2012**, *37*, 1694–1696. [CrossRef] [PubMed]
34. Nesterov, A.V.; Niziev, V.G. Laser beams with axially symmetric polarization. *J. Appl. Phys.* **2000**, *33*, 1817–1822. [CrossRef]
35. Zhou, J.; Yang, L.; Wang, S.; Zhou, J. Minimized spot of annular radially polarized focusing beam. *Opt. Lett.* **2013**, *38*, 1331–1333.
36. Milione, G.; Sztul, H.I.; Nolan, D.A.; Alfano, R.R. Higher-Order Poincaré Sphere, Stokes Parameters, and the Angular Momentum of Light. *Phys. Rev. Lett.* **2011**, *107*, 053601. [CrossRef]
37. Holleczek, A.; Aiello, A.; Gabriel, C.; Marquardt, C.; Leuchs, G. Classical and quantum properties of cylindrically polarized states of light. *Opt. Express* **2011**, *19*, 9714–9736. [CrossRef] [PubMed]
38. Roxworthy, B.J.; Toussaint, K.C.J. Optical trapping efficiencies from n-phase cylindrical vector beams. *Proc. SPIE* **2011**, *7950*, 2362–2375.
39. Zhao, Z.; Wang, J.; Li, S.; Willner, A.E. Metamaterials-based broadband generation of orbital angular momentum carrying vector beams. *Opt. Lett.* **2013**, *38*, 932–934. [CrossRef]
40. Qiu, C.; Palima, D.; Novitsky, A.; Gao, D.; Ding, W.; Zhukovsky, S.V.; Gluckstad, J. Engineering light-matter interaction for emerging optical manipulation applications. *Nanophotonics* **2014**, *3*, 181–201. [CrossRef]
41. Yi, X.; Liu, Y.; Ling, X.; Zhou, X.; Ke, Y.; Luo, H.; Wen, S.; Fan, D. Hybrid-order Poincare sphere. *Phys. Rev. A* **2015**, *91*, 023801. [CrossRef]
42. Schmitz, C.H.J.; Spatz, J.P.; Curtis, J.E. High-precision steering of holographic optical tweezers. *Opt. Express* **2005**, *13*, 8678–8685. [CrossRef] [PubMed]
43. Grier, D.G. A revolution in optical manipulation. *Nature* **2003**, *424*, 810–816. [CrossRef] [PubMed]
44. Cizmar, T.; Dalgarno, H.I.C.; Ashok, P.C.; Gunn-Moore, F.J.; Dholakia, K. Interference-free superposition of nonzero order light modes: Functionalized optical landscapes. *Appl. Phys. Lett.* **2011**, *98*, 081114. [CrossRef]
45. Curtis, E.; Grier, G. Modulated optical vortices. *Opt. Lett.* **2003**, *28*, 872–874. [CrossRef] [PubMed]
46. Han, W.; Yang, Y.; Cheng, W.; Zhan, Q. Vectorial optical field generator for the creation of arbitrarily complex fields. *Opt. Express* **2013**, *21*, 20692–20706. [CrossRef] [PubMed]
47. Moreno, I.; Davis, J.A.; Hernandez, T.M.; Cottrell, D.M.; Sand, D. Complete polarization control of light from a liquid crystal spatial light modulator. *Opt. Express* **2012**, *20*, 364–376. [CrossRef] [PubMed]
48. Chen, S.; Zhou, X.; Liu, Y.; Ling, X.; Luo, H. Generation of arbitrary cylindrical vector beams on the higher order Poincare sphere. *Opt. Lett.* **2014**, *39*, 5274–5276. [CrossRef]

49. Maurer, C.; Jesacher, A.; Fürhapter, S.; Bernet, S.; Ritsch-Marte, M. Tailoring of arbitrary optical vector beam. *New J. Phys.* **2007**, *9*, 78. [CrossRef]
50. Tripathi, S.; Toussaint, K.C. Versatile generation of optical vector fields and vector beams using a non-interferometric approach. *Opt. Express* **2012**, *20*, 10788–10795. [CrossRef] [PubMed]
51. Chensheng, W.; Jonathan, K.; Rzasa, J.R.; Paulson, D.A.; Davis, C.C. Phase and amplitude beam shaping with two deformable mirrors implementing input plane and Fourier plane phase modifications. *Appl. Opt.* **2018**, *57*, 2337–2345.
52. Lou, S.; Zhou, Y.; Yuan, Y.; Lin, T.; Fan, F.; Wang, X.; Huang, H.; Wen, S. Generation of arbitrary vector vortex beams on hybrid-order Poincaré sphere based on liquid crystal device. *Opt. Express* **2019**, *27*, 8596–8604. [CrossRef] [PubMed]
53. Gregg, P.; Mirhosseini, M.; Rubano, A.; Marrucci, L.; Karimi, E.; Boyd, R.W.; Ramachandran, S. Q-plates as higher order polarization controllers for orbital angular momentum modes of fiber. *Opt. Lett.* **2015**, *40*, 1729–1732. [CrossRef] [PubMed]
54. Darryl, N.; Filippus, S.R.; Dudley, A.; Litvin1, I.; Piccirillo, B.; Marucci, L.; Forbes, A. Controlled generation of higher-order Poincare sphere beams from a laser. *Nat. Photonics* **2016**, *10*, 327–332.
55. Liu, Z.; Liu, Y.; Ke, Y.; Liu, Y.; Shu, W.; Luo, H.; Wen, S. Generation of arbitrary vector vortex beams on hybrid-order Poincaré sphere. *Photonics Res.* **2017**, *1*, 19–25. [CrossRef]
56. Liu, Y.; Ling, X.; Yi, X.; Zhou, X.; Luo, H.; Wen, S. Realization of polarization evolution on higher-order Poincare sphere with metasurface. *Appl. Phys. Lett.* **2014**, *104*, 1–4. [CrossRef]
57. Birks, T.A.; Gris-Sánchez, I.; Yerolatsitis, S.; Leon-Saval, S.G.; Thomson, R.R. The photonic lantern. *Adv. Opt. Photonics* **2015**, *7*, 107–167. [CrossRef]
58. Park, K.J.; Song, K.Y.; Kim, Y.K.; Lee, J.H.; Kim, B.Y. Broadband mode division multiplexer using all-fiber mode selective couplers. *Opt. Express* **2016**, *24*, 3543–3549. [CrossRef]
59. Zhao, Y.; Chen, H.; Fontaine, N.K.; Li, J.; Ryf, R.; Liu, Y. Broadband and low-loss mode scramblers using CO_2-laser inscribed long-period gratings. *Opt. Lett.* **2018**, *43*, 2868–2871. [CrossRef]
60. Jiang, Y.; Ren, G.; Lian, Y.; Zhu, B.; Jin, W.; Jian, S. Tunable orbital angular momentum generation in optical fibers. *Opt. Lett.* **2016**, *41*, 3535–3538. [CrossRef]
61. Zeng, X.; Li, Y.; Mo, Q.; Li, W.; Tian, Y.; Liu, Z.; Wu, J. Experimental Investigation of LP11 Mode to OAM Conversion in Few Mode-Polarization Maintaining Fiber and the Usage for All Fiber OAM Generator. *IEEE Photonics J.* **2017**, *8*, 1–7.
62. Jiang, Y.; Ren, G.; Shen, Y.; Xu, Y.; Jin, W.; Wu, Y.; Jian, W.; Jian, S. Two-dimensional tunable orbital angular momentum generation using a vortex fiber. *Opt. Lett.* **2017**, *42*, 5014–5017. [CrossRef] [PubMed]
63. Li, S.; Mo, Q.; Hu, X.; Du, C.; Wang, J. Controllable all-fiber orbital angular momentum mode converter. *Opt. Lett.* **2015**, *40*, 4376–4379. [CrossRef] [PubMed]
64. Bozinovic, N.; Golowich, S.; Kristensen, P.; Ramachandran, S. Control of orbital angular momentum of light with optical fibers. *Opt. Lett.* **2012**, *37*, 2451–2453. [CrossRef] [PubMed]
65. Yao, S.; Ren, G.; Shen, Y.; Jiang, Y.; Zhu, B.; Jian, S. Tunable Orbital Angular Momentum Generation Using All-Fiber Fused Coupler. *IEEE Photonics Tech. Lett.* **2017**, *30*, 99–102. [CrossRef]
66. Jiang, Y.; Ren, G.; Li, H.; Tang, M.; Jin, W.; Jian, W.; Jian, S. Tunable Orbital Angular Momentum Generation Based on Two Orthogonal LP Modes in Optical Fibers. *IEEE Photonics Tech. Lett.* **2017**, *29*, 901–904. [CrossRef]
67. Sihan, W.; Yan, L.; Lipeng, F.; Li, W.; Qiu, J.; Zuo, Y.; Hong, X.; Yu, H.; Chen, R.; Giles, I.P.; et al. Continuously tunable orbital angular momentum generation controlled by input linear polarization. *Opt. Lett.* **2018**, *43*, 2130–2133.

© 2019 by the authors. Licensee MDPI, Basel, Switzerland. This article is an open access article distributed under the terms and conditions of the Creative Commons Attribution (CC BY) license (http://creativecommons.org/licenses/by/4.0/).